Monthly Notices of the ROYAL ASTRONOMICAL SOCIETY

MNRAS **481,** 1597–1608 (2018) doi:10.1093/mnras/sty2308
Advance Access publication 2018 August 28

Off-axis emission of short GRB jets from double neutron star mergers and GRB 170817A

Jonathan Granot,[1★] Ramandeep Gill,[1,2★] Dafne Guetta[3] and Fabio De Colle[4]

[1]*Department of Natural Sciences, The Open University of Israel, 1 University Road, POB 808, Raanana 4353701, Israel*
[2]*Physics Department, Ben-Gurion University, POB 653, Beer-Sheva 84105, Israel*
[3]*ORT-BRAUDE College, Snunit 51, 2161002 Karmiel, Israel*
[4]*Instituto de Ciencias Nucleares, Universidad Nacional Autónoma de México, A.P. 70-543 04510 D.F., Mexico*

Accepted 2018 August 21. Received 2018 August 20; in original form 2017 November 28

ABSTRACT

The short-duration ($\lesssim$ 2 s) GRB 170817A in the nearby ($D \approx 40$ Mpc) elliptical galaxy NGC 4993 is the first electromagnetic counterpart of the first gravitational wave detection of a binary neutron-star (NS–NS) merger. It was followed by optical, IR, and UV emission from half a day up to weeks after the event, as well as late time X-ray to radio emission. The early UV, optical, and IR emission showed a quasi-thermal spectrum suggestive of radioactive-decay powered kilonova-like emission. The late onset of the X-ray (8.9 d) and radio (16.4 d) afterglow emission, together with the low isotropic equivalent γ-ray energy output ($E_{\gamma,\,\rm iso} \approx 5 \times 10^{46}$ erg), strongly suggest emission from a narrow relativistic jet viewed off-axis, initially dominated by low-energy material along our line of sight and gradually overtaken by the more energetic parts of the jet near its core. Here, we set up a general framework for off-axis GRB jet afterglow emission, comparing analytic and numerical approaches, and showing their general predictions for short-hard GRBs that accompany binary NS mergers. The prompt GRB emission suggests a viewing angle well outside the jet's core, and we compare the afterglow light curves expected in such a case to the X-ray, optical, and radio emission from GRB 170817A. We fit the data using a simulation-based off-axis relativistic jet afterglow model featuring an initially top-hat jet, and find a satisfactory fit for a viewing angle to initial jet half-opening angle ratio of $\theta_{\rm obs}/\theta_0 \approx 3$, or $\theta_{\rm obs} \approx 17^\circ(\theta_0/0.1)$.

Key words: gravitational waves – hydrodynamics – gamma-ray burst: general – stars: jets – stars: neutron – ISM: jets and outflows.

1 INTRODUCTION

Gravitational waves (GWs) were first detected only 2 yr ago, and a century after they were predicted by Albert Einstein, by the Advanced Laser Interferometer Gravitational-wave Observatory (LIGO; Abbott et al. 2016a). This first detection was from two coalescing black holes (BHs), and it has recently led to the award of a Nobel prize (the 2017 prize in physics to Rainer Weiss, Barry C. Barish, and Kip S. Thorne). This groundbreaking discovery marked the dawn of a new era of GW astronomy. It was quickly followed by two other BH–BH mergers, and recently yet another one that was also detected by VIRGO (Abbott et al. 2017a). This has clearly established the ability and sensitivity of current GW detectors to robustly and securely detect such sources (merging BHs of a few tens of solar masses) out to ∼Gpc distances. Moreover, LIGO is also capable of detecting GWs from compact binary mergers involving neutron stars (NSs), namely NS–NS and NS–BH, at a volume-weighted mean distance of ~ 70 and ~ 110 Mpc, respectively, and has set an upper limit of 12 600 Gpc^{-3} yr^{-1} on the NS–NS merger rate (90 per cent CL; Abbott et al. 2016b).

However, no significant electromagnetic emission is generally expected for a BH–BH merger (in most scenarios). None the less, its detection is of great importance in NS–NS or NS–BH mergers, which have been suggested to be the progenitors of short-hard γ-ray bursts (SGRBs; e.g. Eichler et al. 1989; Narayan, Paczynski & Piran 1992). An NS–NS merger may plausibly lead to the formation of a BH, which is possibly preceded by a short-lived hypermassive neutron star (HMNS). Accretion on to the BH then launches a relativistic jet (e.g. Rezzolla et al. 2011) that eventually reaches bulk Lorentz factors $\Gamma \gtrsim 100$ and power an SGRB – a short ($\lesssim$ 2 s) intense burst of γ-rays with a characteristic (peak νF_ν) photon energy $E_{\rm pk} \sim 400$ keV and isotropic-equivalent γ-ray energy output $E_{\gamma,\rm iso} \simeq 10^{49}$–$10^{51}$ erg (Nakar 2007; Berger 2014). GRBs of the long-soft class, on the other hand, are known to originate from

★ E-mail: granot@openu.ac.il (JG); rsgill.rg@gmail.com (RG)

the death of massive stars, and are found to be associated with star-forming regions and type Ic core-collapse supernovae (e.g. Woosley & Bloom 2006).

The detection of an SGRB, GRB 170817A (von Kienlin, Meegan & Goldstein 2017), in coincidence with the first GW detection of an NS–NS merger (Abbott et al. 2017b), in the relatively nearby ($D \approx 40$ Mpc) elliptical galaxy NGC 4993, provides the long awaited 'smoking gun' that binary NS mergers indeed give rise to SGRBs. This exciting news led to a huge multiwavelength follow-up effort, involving observations by detectors across the EM spectrum (see e.g. Abbott et al. 2017d and references therein). This source was detected in the optical, UV, and IR after about half a day, as well as in X-rays (after 8.9 d; Troja et al. 2017) and radio (after 16.4 d; Hallinan et al. 2017) that took advantage of the much better position measurement from the preceding optical detections. All these measurements provide critical information regarding the jet geometry, merger ejecta, and *r*-process elements (e.g. Rosswog, Piran & Nakar 2013).

The optical and radio detections allowed to pinpoint the source's location, which was found to be about 2 kpc in projection from the centre of NGC 4993. In the Appendix, we use the projected distance to show that the binary could not have moved in a straight line from its birth site to its merger site.

A binary NS merger can produce EM radiation over a wide range of wavelengths and time-scales. During an NS–NS (or NS–BH) merger some sub-relativistic ejecta (of mass $\sim 10^{-3}$–$10^{-2}\,\mathrm{M}_{\odot}$) is thought to be thrown out along the orbital plane at a modest fraction of the speed of light, $\beta = v/c \sim 0.1$–0.3. Rapid neutron capture in the sub-relativistic ejecta (e.g. Lattimer & Schramm 1976) is hypothesized to produce a kilonova (also known as a macronova or mini-supernova) – a UV, optical and near-infrared signal lasting hours to weeks (e.g. Li & Paczyński 1998) powered by radioactive decay. Eventually, this sub-relativistic ejecta is decelerated significantly by sweeping up mass comparable to its own, and transfers most of its kinetic energy ($\sim 10^{50}$–10^{51} erg) to the swept up shocked ambient medium. The latter produces radio emission through synchrotron radiation, which typically peaks on a time-scale of months to years after the merger (e.g. Nakar & Piran 2011).

Another source of dynamical ejecta during an NS–NS merger is the collision between the two NSs that drives a strong shock into them, which accelerates as it reaches the sharp density gradient in their outer layer, thus producing a quasi-spherical ultra-relativistic outflow, which may give rise to detectable emission in X-rays (peaking promptly), optical (peaking within seconds) and radio (peaking within several hours to a day) (Kyutoku, Ioka & Shibata 2014). The mildly relativistic tail of this ejecta, which contains a good fraction of its mass, may both contribute to the kilonova as well as potentially be harder for the jet to bore through because it is more isotropic compared to the tidal tails that reside predominantly in the orbital plane. Finally, it has also been suggested that several seconds prior to or tens of minutes after the merger, one might detect a coherent radio burst lasting milliseconds (e.g. Hansen & Lyutikov 2001; Zhang 2014).

If a short-lived ($\lesssim 1$ s) HMNS is formed during the merger, then its slightly delayed (relative to the NS–NS merger) collapse triggers the formation of a relativistic jet. In this case, the jet needs to bore its way through both the neutrino-driven wind that was launched before this collapse and the dynamical ejecta from the NS–NS merger. The jet propagation within the medium in the immediate vicinity of the merger site forms a cocoon (e.g. Lazzati et al. 2017a; Nakar & Piran 2017) whose cooling and radioactive decay signatures may produce observable emission in the optical-UV on time-scales of an hour or so (Gottlieb, Nakar & Piran 2018). The delayed collapse and the time it takes for the jet to bore through the wind may potentially account (e.g. Granot, Guetta & Gill 2017) for the delay of 1.74 ± 0.05 s between the GW chirp signal and the GRB prompt emission onset (Abbott et al. 2017e).

If the relativistic jet that forms after the NS–NS merger happens to point towards us, then we may observe a short prompt γ-ray emission episode from an SGRB, lasting $\lesssim 2$ s, followed by afterglow emission in X-ray, optical, and radio lasting for hours, days, or weeks (e.g. Eichler et al. 1989; Narayan et al. 1992; Nakar 2007; Berger 2014; Fong et al. 2015). However, in most cases the relativistic jet will not point towards us, and in this work, we will focus on the observable signatures that are expected in that case.

The search for orphan afterglows – afterglows that are not associated with observed prompt GRB emission – has immediately followed the realization that GRBs are beamed with rather narrow opening angles, while the afterglow itself could be observed over a wider angular range. Rhoads (1997) was the first to suggest that observations of orphan afterglows would enable us to estimate the opening angles and the true rate of GRBs. Because of relativistic beaming, only a region of angular size $1/\Gamma$ around the line of sight is visible. Therefore, when a jet of initial half-opening angle $\theta_0 > 1/\Gamma$ points towards us then initially we cannot notice that it is indeed a jet and not part of a spherical flow. This is typically valid during the prompt γ-ray emission, and we can learn that it is indeed a jet only later during the afterglow stage when the jet decelerates whereby its Lorentz factor Γ drops below $1/\theta_0$, resulting in an achromatic steepening of the flux decay rate, known as a jet break (Rhoads 1999; Sari, Piran & Halpern 1999).

When a jet is viewed off-axis, from outside of its initial aperture, at a viewing angle $\theta_{\rm obs} > \theta_0$, then its prompt γ-ray emission is significantly suppressed and would in most cases be missed, unless the GRB is particularly bright, nearby, or viewed from very close to its edge, such that $\Gamma(\theta_{\rm obs} - \theta_0) \lesssim$ a few. However, the afterglow emission becomes visible once the beaming cone of the afterglow radiation reaches our line of sight. The jet's beaming cone subtends an angle of $\theta_j + 1/\Gamma$ from its symmetry axis, the first term (θ_j) is geometrical (since due to relativistic beaming the brightest part of the jet is the one closest to our line of sight) and can grow with time by up to $\theta_j \leq \theta_0 + 1/\Gamma$ to the extent that the jet expands sideways. The second term ($1/\Gamma$) arises from relativistic beaming. Altogether, for $\theta_{\rm obs} \gtrsim 2\theta_0$ the beaming cone reaches the line of sight when Γ drops to $\sim 1/\theta_{\rm obs}$, at which the light curve peaks, and subsequently approaches that for an on-axis observer.

For a jet sideways expansion at close to its sound speed θ_j grows exponentially with radius after the jet break radius (Rhoads 1999; Sari et al. 1999). While noticeable deviations from this scaling are expected for $\theta_j \gtrsim 0.1$ (Granot & Piran 2012), the resulting analytic light curve scalings are still very useful also for $\theta_{\rm obs} \gtrsim 0.1$. This results in a post jet break dynamics and therefore light curves that are universal, in the sense that they are independent of θ_0, and depend only on the jet's true energy E rather than on its isotropic equivalent energy (Granot et al. 2002). Here, we follow and generalize the result of Nakar, Piran & Granot (2002) for the calculation of these post jet break light curves and peak time and flux for off-axis observers.

In Section 2, we briefly describe the light curve and spectral behavior of ultraviolet (UV), optical, and near-infrared (IR) emission from the kilonova associated to GRB 170817A and mention the requirement for a two component ejecta to explain the blue and red components of the emission. In Section 3, we outline a simple analytic model for off-axis afterglow emission, which provides the peak time and flux for light curves seen by observers outside of the jet's initial aperture. The general predictions of this model (for $\theta_{\rm obs} \gtrsim 2\theta_0$) are presented in Section 4. In Section 5, we present numerical light curves from relativistic hydrodynamic simulations of a GRB jet during the afterglow phase, and compare them to the predictions of the simple analytic model. Next, we directly compare the numerical light curves from hydrodynamic simulations to the data for GRB 170817A in Section 6. For light curve fitting, we use up-to-date observations, and ignore the early IR, optical, and UV data since they are dominated by kilonova emission. For the purpose of detailed comparison with the data, given the moderately large number of model parameters and corresponding parameter space to explore, we use scaling relations of the dynamical equations in order to avoid the need for performing a large number of hydrodynamic simulations. Finally, we summarize our main findings in Section 7 and discuss their implications in Section 8.

2 IR, OPTICAL, AND UV KILONOVA EMISSION IN GRB 170817A

The optical counterpart to GRB 170817A, initially designated as SSS17a, was discovered at 10.87 h post-merger (Coulter et al. 2017); the designation of the source was later changed to AT 2017gfo. Soon after it was followed up by rapid observations in the UV and IR, which revealed a quasi-thermal spectrum (e.g. Abbott et al. 2017d) that was consistent with the expected kilonova emission. However, it was interesting to note that after ∼2 d the emission in the UV and blue optical bands started to decline rapidly and the spectrum showed a gradual shift towards redder bands. At the same time, the IR emission showed a much shallower decline that lasted for up to ∼8 d, after which it started to decline rapidly as well (e.g. Arcavi et al. 2017; Cowperthwaite et al. 2017; Drout et al. 2017; Evans et al. 2017; Kasliwal et al. 2017; Kilpatrick et al. 2017; Pian et al. 2017; Shappee et al. 2017; Smartt et al. 2017; Troja et al. 2017).

A kilonova or macronova is a general term for quasi-thermal emission powered by the radioactive decay in sub-relativistic neutron-rich material that is ejected during an NS–NS or NS–BH merger. During and following a double NS merger, a small fraction of the system's mass ($M_{\rm ej} \sim 10^{-4}$–$10^{-2}\,{\rm M}_\odot$ for NS–NS or up to $10^{-1}\,{\rm M}_\odot$ for NS–BH) is expected to be ejected at mildly relativistic speeds ($\beta_{\rm ej} \sim 0.1$–0.3) and produce EM emission due to the heating by radioactive decay of r-process elements. Models describing this process are still rather uncertain. Below we discuss some of the basic properties of such models, and their ability to account for the optical to IR emission in GRB 170817A.

Tidal and hydrodynamic interactions are expected to produce a 'dynamical' ejecta that is highly neutron rich with electron fraction $Y_{\rm e} \lesssim 0.1$. The generation of elements with mass number above 130 and in particular Lanthanides (with an atomic number $57 \leq Z \leq 71$) by r-process nucleosynthesis within this ejecta leads to high opacity ($\kappa > 1\,{\rm cm^2\,g^{-1}}$) and hence to a relatively low peak luminosity, $L_{\rm peak} \sim 10^{40}$–$10^{41}\,{\rm erg\,s^{-1}}$, with a temperature in the IR range, $kT_{\rm eff}(t_{\rm peak}) \sim 0.2$ eV, and a peak time $t_{\rm peak} \sim$ a few days (the so-called red kilonova). The spectrum of the kilonova can be fitted with a blackbody spectrum. Fitting this spectrum to the data provides how the bolometric luminosity, the black body temperature, and radius evolve with time.

The peak time $t_{\rm peak}$ occurs when the photon diffusion time through the ejecta equals the dynamical time, and it thus depends on $M_{\rm ej}$, $\beta_{\rm ej}$, and κ. The peak luminosity, $L_{\rm peak}$, is set by the radioactive decay rate at $t_{\rm peak}$, which depends on the ejecta's mass ($M_{\rm ej}$) and composition such that (Metzger et al. 2010; Metzger & Fernandez 2014)

$$L_{\rm peak} = 5\times 10^{41} f_{-6}\beta_{-1}^{1/2} M_{-2}^{1/2}\kappa_0^{-1/2}\,{\rm erg\,s^{-1}}, \tag{1}$$

$$t_{\rm peak} = 1.4\beta_{-1}^{-1/2} M_{-2}^{1/2}\kappa_0^{1/2}\,{\rm d}, \tag{2}$$

where $f = Q_{\rm heat}/(M_{\rm ej}c^2)$ quantifies the amount of energy deposited into heat by the radioactive decay per unit ejecta rest energy, $\beta_{-1} = \beta_{\rm ej}/0.1$, $M_{-2} = M_{\rm ej}/10^{-2}\,{\rm M}_\odot$, and the ejecta's opacity is $\kappa = \kappa_0\,{\rm cm^2\,g^{-1}}$. Here and what follows, the notation Q_x denotes the value of the quantity Q in units of 10^x times its (cgs) units.

The comparison of model light curves with the UV–optical–IR data from GRB 170817A lead to the realization that a single-component kilonova model does not provide a good fit to the data, and instead two distinct components are needed (e.g. Cowperthwaite et al. 2017; Kasen et al. 2017). One 'blue' component that fits the early optical emission is Lanthanide poor and has $M_{\rm ej} \approx 0.01\,{\rm M}_\odot$ and $\beta_{\rm ej} \approx 0.3$, while the second, 'red' component that fits the later optical to IR data is Lanthanide rich with $M_{\rm ej} \approx 0.04\,{\rm M}_\odot$ and $\beta_{\rm ej} \approx 0.1$. This type of separation where the blue and red emission components occupy distinct parts of the outflow, such as the polar and equatorial regions respectively, was already explored before this event in some kilonova models (e.g. Kasen, Fernandez & Metzger 2015; Metzger 2017).

2.1 The late time radio emission from the sub-relativistic ejecta

The emission from the interaction of the sub-relativistic ejecta with the external medium was studied by Nakar & Piran (2011). They find that for sufficiently high radio frequencies (typically $\nu \gtrsim 1$ GHz) this emission peaks at the deceleration time $t_{\rm dec}$ and flux density given by

$$t_{\rm dec} = 0.77 E_{49}^{1/3} n_0^{-1/3}(3\beta_0)^{-5/3}\,{\rm yr}, \tag{3}$$

$$F_\nu^{\rm peak} \approx 0.25 E_{49} n_0^{\frac{p+1}{4}} \epsilon_{B,-1}^{\frac{p+1}{4}} \epsilon_{{\rm e},-1}^{p-1} (3\beta_0)^{\frac{5p-7}{2}} D_{\rm 40Mpc}^{-2} \nu_{9.93}^{\frac{1-p}{2}}\,{\rm mJy}, \tag{4}$$

where we have used a fiducial distance of $D = 40D_{\rm 40Mpc}$ Mpc, initial dimensionless velocity $\beta_0 = 1/3$, a frequency of $\nu = 8.46\,\nu_{9.93}$ GHz, and the circumburst medium density $n = n_0\,{\rm cm^{-3}}$. Also, a fraction ε_B of the total internal energy density just behind the shock goes into the magnetic field. A fraction $\varepsilon_{\rm e}$ is given to the shock heated relativistic power-law electrons with distribution ${\rm d}N_{\rm e}/{\rm d}\gamma_{\rm e} \propto \gamma_{\rm e}^{-p}$ for $\gamma_{\rm m} \leq \gamma_{\rm e} \leq \gamma_M$. The above equations assume a spherical outflow, but if the same outflow (of same β_0 and total energy E) is directed into a small fraction f_Ω of the total solid angle, this would correspond, until the deceleration time, to a part of a spherical flow with $E_{\rm k,iso} = E/f_\Omega$ thus increasing $t_{\rm dec}$ by a factor of $f_\Omega^{-1/3}$ and hardly affecting[1] $F_\nu^{\rm peak}$. For lower frequencies the peak time can occur later, at the passage of $\nu_{\rm m}$ or ν_a, whichever occurs later. Therefore, for GRB 170817A the peak of this emission might be expected on a time-scale of roughly a few to several years, but it may still be detectable (perhaps even somewhat before the peak time) for high enough values of n_0, ε_B, and $\varepsilon_{\rm e}$.

The emission from the sub-relativistic ejecta is expected to dominate at $t \gtrsim t_{\rm dec}$ over the radio afterglow from the (originally) relativistic jet if indeed its true energy is larger, since by that time both

[1] If $F_\nu^{\rm peak} \propto E^a$ then it would change as $F_\nu^{\rm peak}(E) \to f_\Omega F_\nu^{\rm peak}(E/f_\Omega) = f_\Omega^{1-a} F_\nu^{\rm peak}(E)$, where $a = 1$ for high enough radio frequencies, and it is not very far from 1 even at lower frequencies.

outflows would be Newtonian and radiate (almost) isotropically, and the more energetic of the two is expected to produce a higher radio flux.

3 SIMPLE ANALYTIC MODEL FOR OFF-AXIS EMISSION FROM GRB JETS

Following Nakar et al. (2002), we consider an adiabatic double-sided jet with a total energy E and an initial opening angle θ_0, and a simple hydrodynamic model for the jet evolution (Rhoads 1999; Sari et al. 1999). Initially, as long as $\Gamma > 1/\theta_0$, the jet propagates as if it were spherical with an equivalent isotropic energy of $2E/\theta_0^2$:

$$E = \frac{2\pi}{3}\theta_j^2 R^3 \Gamma^2 n m_{\rm p} c^2 \tag{5}$$

with $\theta_j \approx \theta_0$, where n is the ambient number density, $m_{\rm p}$ is the proton mass, and c is the speed of light. The spherical phase ends once Γ drops below $1/\theta_0$, at which point the jet expands sideways relativistically in its own rest frame, leading to $\theta_j \sim 1/\Gamma$ and

$$E = \frac{2\pi}{3} R^3 n m_{\rm p} c^2, \tag{6}$$

where the shock radius remains almost constant.[2] The evolution in this phase is independent of θ_0, which only determines the jet break time, t_j. The light curves depend only on E and n, along with the shock microscopic parameters (the equipartition parameters, ϵ_B, $\epsilon_{\rm e}$, and the power-law index p of the electron distribution). During both phases the observed time is given by

$$t = (1+z)\frac{R}{4c\Gamma^2}\,. \tag{7}$$

Equations (6) and (7) yield that the jet break transition takes place at (Sari et al. 1999),

$$t_j = 0.70(1+z)\left(\frac{E_{51}}{n_0}\right)^{1/3}\left(\frac{\theta_0}{0.1}\right)^2\ \mathrm{d}. \tag{8}$$

Because of relativistic beaming, an observer located at $\theta_{\rm obs}$ outside the initial opening angle of the jet ($\theta_{\rm obs} > \theta_0$) will (practically) observe the afterglow emission only near its peak at t_θ when $\Gamma = 1/\theta_{\rm obs}$:

$$t_{\rm peak}(\theta_{\rm obs}) = A\left(\frac{\theta_{\rm obs}}{\theta_0}\right)^2 t_j = 70(1+z)A\left(\frac{E_{51}}{n_0}\right)^{1/3}\theta_{\rm obs}^2\ \mathrm{d}. \tag{9}$$

The flux rises until it peaks at $t_{\rm peak}$ and subsequently decays in the same way as for an on-axis observer. The factor A in equation (9) is of the order of unity and will be taken as 1 following Nakar et al. (2002).

The synchrotron slow cooling ($\nu_{\rm m} < \nu_{\rm c}$) light curve for the initial (spherical) phase was derived by Sari, Piran & Narayan (1998) and refined by Granot & Sari (2002). Sari et al. (1999) provide temporal scalings for the maximal flux and the typical synchrotron ($\nu_{\rm m}$) and cooling ($\nu_{\rm c}$) frequencies during the modified hydrodynamic evolution after the jet break. Combining both results, using the Granot & Sari (2002) normalization for the fluxes and typical frequencies, one obtains the universal post jet-break light curve (Nakar et al. 2002) for an on-axis observer, where for convenience the frequency is normalized to the optical (5×10^{14} Hz). The flux above the self-absorption frequency is given by

$$F_{\nu>\nu_{\rm c},\nu_{\rm m}}(t) = 0.459\frac{g_0(p)}{g_0(2.2)}10^{\frac{2.2-p}{3.93}}(1+z)^{\frac{p+2}{2}}D_{\rm L28}^{-2}(1+Y)^{-1} \times \epsilon_{\rm e,-1}^{p-1}\epsilon_{B,-2}^{\frac{p-2}{4}}n_0^{\frac{-p-2}{12}}E_{50.7}^{\frac{p+2}{3}}t_{\rm d}^{-p}\nu_{14.7}^{-p/2}\ \mathrm{mJy}, \tag{10}$$

$$F_{\nu_{\rm m}<\nu<\nu_{\rm c}}(t) = 0.170\frac{g_1(p)}{g_1(2.2)}10^{\frac{2.2-p}{3.93}}(1+z)^{\frac{p+3}{2}}D_{\rm L28}^{-2} \times \epsilon_{\rm e,-1}^{p-1}\epsilon_{B,-2}^{\frac{p+1}{4}}n_0^{\frac{3-p}{12}}E_{50.7}^{\frac{p+3}{3}}t_{\rm d}^{-p}\nu_{14.7}^{(1-p)/2}\ \mathrm{mJy}, \tag{11}$$

$$F_{\nu_a<\nu<\nu_{\rm m}<\nu_{\rm c}}(t) = 3.62\frac{g_2(p)}{g_2(2.2)}(1+z)^{5/3}D_{\rm L28}^{-2} \times \epsilon_{\rm e,-1}^{-2/3}\epsilon_{B,-2}^{1/3}n_0^{2/9}E_{50.7}^{10/9}t_{\rm d}^{-1/3}\nu_{9.93}^{1/3}\ \mathrm{mJy}, \tag{12}$$

where $D_{\rm L}$ is the luminosity distance and $g_0(p) \equiv 10^{-0.56p}(p-0.98)[(p-2)/(p-1)]^{p-1}$, $g_1(p) \equiv 10^{-0.31p}(p-0.04)[(p-2)/(p-1)]^{p-1}$, $g_2(p) = (p-1)^{5/3}/[(3p-1)(p-2)^{2/3}]$, and Y is the Compton y-parameter (which is included in the results shown in the figures below). The cooling frequency $\nu_{\rm c}$ and the typical synchrotron frequency of the minimal energy electrons $\nu_{\rm m}$ at $t > t_j$ are given by equating the flux in equation (11) to that in equations (10) and (12), respectively,

$$\nu_{\rm c} = 3.62\times10^{15}\left[\frac{2.16}{1.22}\frac{(p-0.98)}{(p-0.04)}\right]^2 10^{\frac{2.2-p}{1.985}}(1+z)^{-1} \times \epsilon_{B,-2}^{-3/2}n_0^{-5/6}E_{50.7}^{-2/3}(1+Y)^{-2}\ \mathrm{Hz}, \tag{13}$$

$$\nu_{\rm m} = 3.74\times10^{11}\left[\frac{g_1(p)g_2(2.2)}{g_1(2.2)g_2(p)}10^{\frac{2.2-p}{3.93}}\right]^{6/(3p-1)}(1+z) \times \epsilon_{B,-2}^{1/2}\epsilon_{\rm e,-1}^{2}n_0^{-1/6}E_{50.7}^{2/3}t_{\rm d}^{-2}\ \mathrm{Hz}. \tag{14}$$

Note that both frequencies are independent of θ_0, and $\nu_{\rm c}$ remains constant in time (at $t > t_j$).

Since the maximal flux occurs near $t_{\rm peak}(\theta_{\rm obs})$ when the off-axis light curve joins that for an on-axis observer, the peak flux for an observer at $\theta_{\rm obs}$ can be obtained by substituting equation (9) into equations (10)–(12),

$$F^{\rm peak}_{\nu>\nu_{\rm c},\nu_{\rm m}}(\theta_{\rm obs}) = 1.67\frac{g_0(p)}{g_0(2.2)}A^{-p}(1+z)^{1-p/2}D_{\rm L28}^{-2} \times (1+Y)^{-1}\epsilon_{\rm e,-1}^{p-1}\epsilon_{B,-2}^{\frac{p-2}{4}}n_0^{\frac{3p-2}{12}}E_{50.7}^{2/3}\nu_{14.7}^{-p/2}\theta_{\rm obs,-1}^{-2p}\ \mathrm{mJy}, \tag{15}$$

$$F^{\rm peak}_{\nu_{\rm m}<\nu<\nu_{\rm c}}(\theta_{\rm obs}) = 0.618\frac{g_1(p)}{g_1(2.2)}A^{-p}(1+z)^{(3-p)/2}D_{\rm L28}^{-2} \times \epsilon_{\rm e,-1}^{p-1}\epsilon_{B,-2}^{\frac{p+1}{4}}n_0^{\frac{p+1}{4}}E_{50.7}\nu_{14.7}^{(1-p)/2}\theta_{\rm obs,-1}^{-2p}\ \mathrm{mJy}. \tag{16}$$

$$F^{\rm peak}_{\nu_a<\nu<\nu_{\rm m}<\nu_{\rm c}}(\theta_{\rm obs}) = 4.40\frac{g_2(p)}{g_2(2.2)}A^{-1/3}(1+z)^{4/3}D_{\rm L28}^{-2} \times \epsilon_{\rm e,-1}^{-2/3}\epsilon_{B,-2}^{1/3}n_0^{1/3}E_{50.7}\nu_{9.93}^{1/3}\theta_{\rm obs,-1}^{-2/3}\ \mathrm{mJy}. \tag{17}$$

The peak flux (which is also independent of θ_0) depends very strongly on $\theta_{\rm obs}$, and quickly decreases when the observer moves away from the jet axis.

In this section, it was implicitly assumed that the observer is initially well outside the edge of the jet, $\theta_{\rm obs} \gtrsim 2\theta_0$. None the less, it can still be generalized to closer lines of sight, $\theta_0 + 1/\Gamma < \theta_{\rm obs} \lesssim 2\theta_0$ or correspondingly $1/\Gamma_0 < \Delta\theta \lesssim \theta_0$ where $\Delta\theta \equiv \theta_{\rm obs} - \theta_0$, as follows. In this case, the peak flux still occurs when the beaming cone reaches the line of sight; however, in this regime,

[2] More detailed calculations show that R increases slowly and Γ decreases exponentially with R (Rhoads 1999; Piran 2000).

it occurs before the jet break time, i.e. while $\Gamma > 1/\theta_0$ and the jet has not yet come into lateral causal contact and therefore has not expanded sideways significantly. Therefore, the jet dynamics may still be approximated as part of a spherical flow with $E_{k,\rm iso} = E/(1-\cos\theta_0) \approx 2E/\theta_0^2$. Using the corresponding expression for $\Gamma(t)$ (e.g. Sari et al. 1998; Granot & Sari 2002; Granot 2012b; Granot & Ramirez-Ruiz 2012) and equating it to $1/\Delta\theta$ one obtains an expression for the peak time in this case,

$$\frac{t_{\rm peak}(1/\Gamma_0 < \Delta\theta \lesssim \theta_0)}{(1+z)} \approx 1.4\times 10^4 \left(\frac{E_{50.7}}{n_0\theta_{0,-1}^2}\right)^{1/3}\left(\frac{\Delta\theta}{0.05}\right)^{8/3}\ {\rm s}. \tag{18}$$

This roughly coincides with equation (9) for $\Delta\theta = \theta_0$, which corresponds to $t_{\rm peak} \sim t_j$. The peak flux can then be obtained by substituting $t = t_{\rm peak}$ from equation (18) in the expression for the on-axis pre-jet break flux density at the relevant PLS of the spectrum (e.g. table 1 of Granot & Sari 2002) corresponding to a spherical flow with $E_{k,\rm iso} \approx 2E/\theta_0^2$.

4 GENERAL PREDICTIONS FOR A NEARBY SHORT-HARD GRB

4.1 Predictions if $\theta_{\rm obs}$ is not known from the GW signal

From the GW observation, the distance D to the source is rather small and therefore we neglect here cosmological redshift and time dilation (effectively using $z = 0$). For the shock microphysical parameters, we choose fiducial values guided by afterglow modelling of both long and short GRBs: $\varepsilon_{\rm e} = 0.1$, $\varepsilon_B = 0.1$, $p = 2.5$. For the external density, we take a value of $n_0 = 1$, typical of the ISM. For the jet energy, we are guided by the typical isotropic equivalent γ-ray energies of SGRB, $E_{\gamma,\rm iso} \sim 10^{49}$–$10^{51}$ erg, and assuming that the jet covers a fraction $\sim 10^{-2}$–10^{-1} of the total solid angle (corresponding to $8^\circ \lesssim \theta_0 \lesssim 26^\circ$), or $E \sim 10^{48}$–10^{49} erg, and take the upper end of this estimated range, $E = 10^{49}$ erg. For illustrative purposes, we assume a distance to the source of $D = 40$ Mpc. We explore the dependence of the peak flux on the most uncertain parameters, namely the external density n, the viewing angle $\theta_{\rm obs}$, the fraction of the internal energy behind the afterglow shock in the magnetic field, ε_B, and the jet energy, E. Semi-analytic modelling of light curves for different viewing angles and from different emission components, namely prompt, afterglow, and the hot cocoon surrounding the relativistic jet, was also done in Lazzati et al. (2017a).

Fig. 1 shows the dependence of the peak flux in X-ray (1 keV), optical (R band) and radio (8.46 GHz) on the external density n and the viewing angle $\theta_{\rm obs}$ as well as on the corresponding peak time, $t_{\rm peak}$. One can quickly read off of it the expected flux for a given observing frequency ν and time t (for $t \gtrsim t_{\rm peak}$), or the expected peak flux for a given viewing angle $\theta_{\rm obs}$, which may potentially be constrained by the GW signal.

Fig. 2 shows the dependence of the peak flux in X-ray, optical, and radio on the magnetic field equipartition parameter ε_B, and on the viewing angle $\theta_{\rm obs}$ or the corresponding peak time, $t_{\rm peak}$.

Fig. 3 shows the dependence of the peak flux X-ray, optical, and radio on the jet energy, E, and on the viewing angle $\theta_{\rm obs}$ or the corresponding peak time, $t_{\rm peak}$.

4.2 More constraints if $\theta_{\rm obs}$ is known from the GW signal

In this subsection, we demonstrate how the constraints on the relevant model parameters can become tighter if the viewing angle

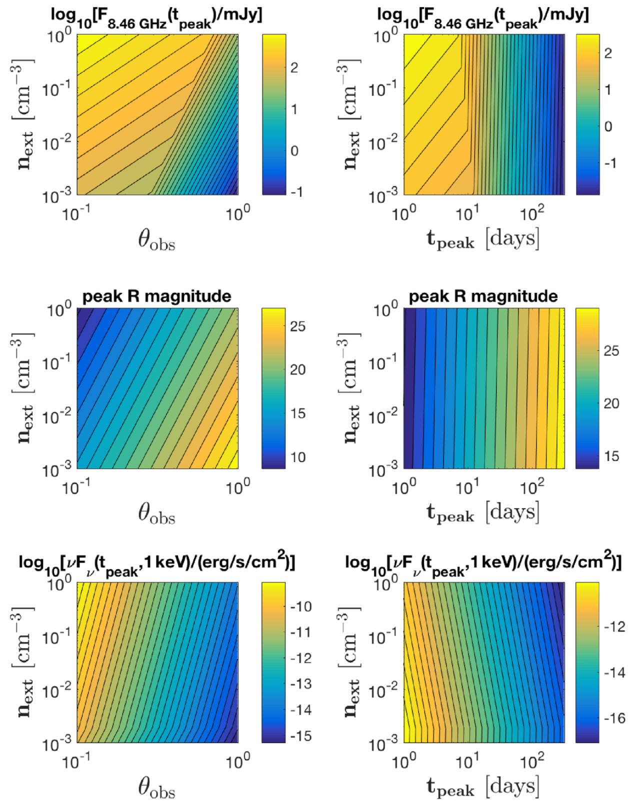

Figure 1. The peak flux in the radio (8.46 GHz; *top panels*), optical (R band; *middle panels*) and X-ray (1 keV; *bottom panels*), for an off-axis observer as a function of the external density $n = n_0\,{\rm cm^{-3}}$ and the viewing angle $\theta_{\rm obs}$ (*left-hand panels*) or the corresponding peak time $t_{\rm peak}$ (*right-hand panels*). The remaining model parameters are $\varepsilon_{\rm e} = \varepsilon_B = 0.1$, $p = 2.5$, $E = 10^{49}$ erg, $D = 40$ Mpc.

$\theta_{\rm obs}$ is determined from the GW signal. The latter may be achieved since the jet axis is expected to be aligned with the spin axis of the BH that is produced during the merger (since both are expected to be aligned with the binary's orbital angular momentum, i.e. normal to the orbital plane), and one can determine from the GW signal the angle of the BH's spin relative to our line of sight, which is identified with $\theta_{\rm obs}$. For concreteness, we will assume values of $\theta_{\rm obs} = 0.6 \pm 0.1$ as a case study.

When $\theta_{\rm obs}$ is measured from the GW signal its value can be used, which reduces the unknown parameter space and allows us to plot contour plots for two intrinsic model parameters, such as n and E as demonstrated in Fig. 4, or n and ε_B as demonstrated in Fig. 5. Larger values of E, n, and ε_B would make the emission from such an off-axis GRB afterglow jet brighter at the peak time of the light curve, $t_{\rm peak}$, and therefore easier to detect. On the other hand, sufficiently low values of these parameters might make such an emission too dim to be detected. The peak time-scales as $t_{\rm peak} \propto (E/n)^{1/3}\theta_{\rm obs}^2$ (see equation 9), and therefore even for a given $\theta_{\rm obs}$, it can vary over a reasonable range for different values of E/n (see the bottom right-hand panel of Fig. 4).

5 OFF-AXIS AFTERGLOW LIGHT CURVES FROM GRB JET SIMULATIONS

The GRB afterglow light curves, and in particular those for off-axis observers ($\theta_{\rm obs} > \theta_0$), strongly depend on the jet dynamics during the afterglow phase. Analytic models have traditionally obtained

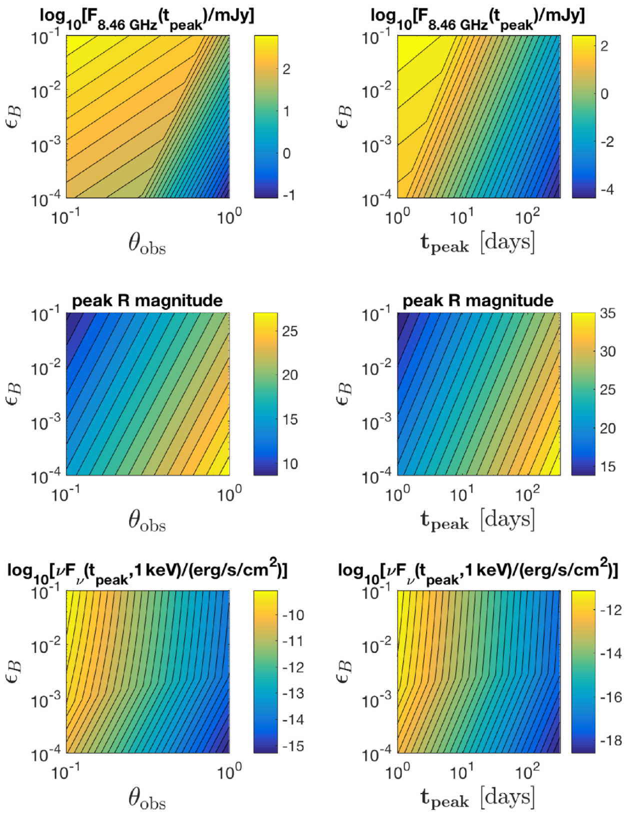

Figure 2. Similar to Fig. 1 but varying the magnetic field equipartition parameter ε_B instead of the external density (with $n_0 = 1$, $\varepsilon_e = 0.1$, $p = 2.5$, $E = 10^{49}$ erg).

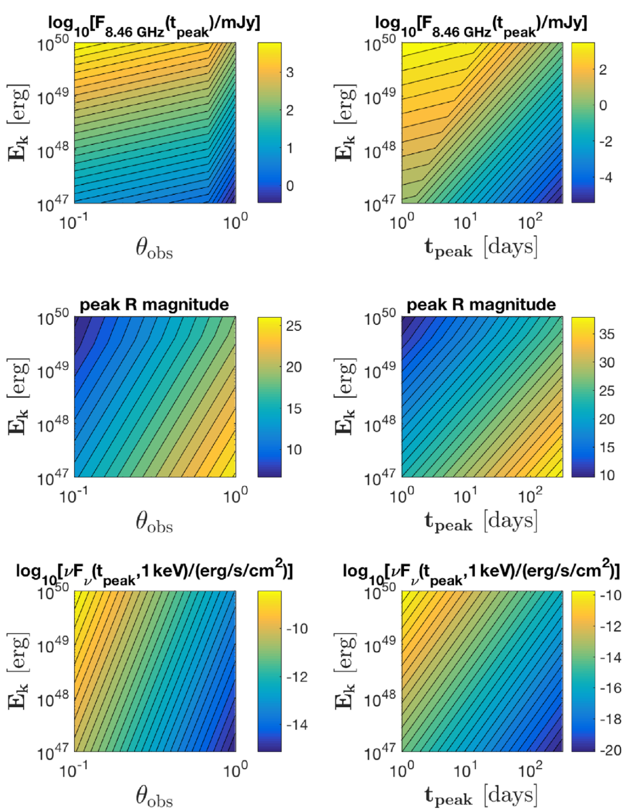

Figure 3. Similar to Fig. 1 but varying the jet energy E instead of the external density (with $n_0 = 1$, $\varepsilon_e = \varepsilon_B = 0.1$, $p = 2.5$).

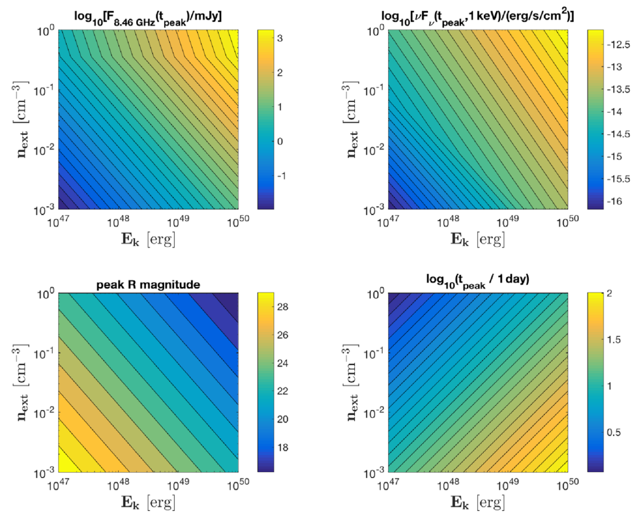

Figure 4. The peak flux in the radio (8.46 GHz; *top panels*), optical (*R* band; *middle panels*) and X-ray (1 keV; *bottom panels*), as well as the time of the peak flux $t_{\rm peak}$, for an off-axis observer at $\theta_{\rm obs} = 0.6$, as a function of the external density $n = n_0\,{\rm cm}^{-3}$ and the jet energy E.

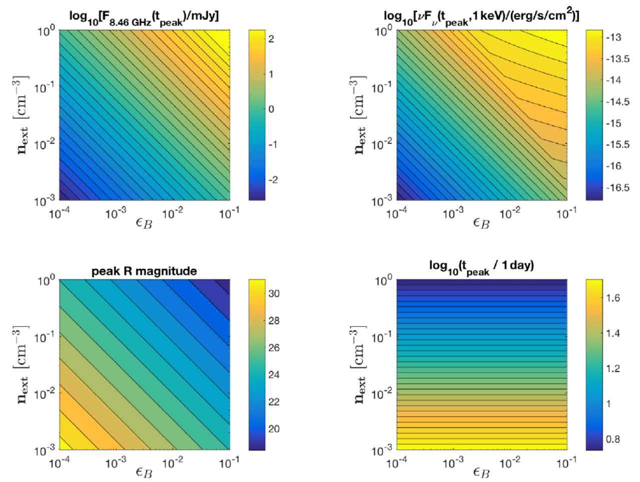

Figure 5. The peak flux in the radio (8.46 GHz; *top panels*), optical (*R* band; *middle panels*) and X-ray (1 keV; *bottom panels*), as well as the time of the peak flux $t_{\rm peak}$, for an off-axis observer at $\theta_{\rm obs} = 0.6$, as a function of the external density $n = n_0\,{\rm cm}^{-3}$ and the magnetic field equipartition parameter ε_B.

an exponential lateral expansion with radius after the jet's Lorentz factor Γ drops below the inverse of its initial half-opening angle θ_0, $1 \ll \Gamma < 1/\theta_0$ (e.g. Rhoads 1999; Sari et al. 1999; Gruzinov 2007; Keshet & Kogan 2015). However, numerical simulations (e.g. Granot et al. 2001; Zhang & MacFadyen 2009) have found that the jet's lateral expansion is much more modest and most of its energy remains within its initial half-opening angle until it becomes mildly relativistic, and only then it starts to gradually approach spherical symmetry (i.e. the Newtonian spherical self-similar Sedov–Taylor solution).

This apparent discrepancy has been reconciled (Wygoda, Waxman & Frail 2011; Granot & Piran 2012) by showing that the simple analytic models strongly rely on the approximations of a small jet half-opening angle ($\theta_j \ll 1$) and ultra-relativistic Lorentz factor ($\Gamma \gg 1$) and break down when the jet is no longer extremely narrow and ultra-relativistic. Rapid, exponential lateral expansion with radius is expected only for jets that are initially extremely narrow, $\theta_0 \ll 10^{-1.5}$ (Granot & Piran 2012). Inferred values of θ_0 in GRBs are typically not that small, and therefore a more modest lateral expansion is expected, as seen in numerical simulations.

Moreover, simulations also show that the jet is not uniform as assumed for simplicity in analytic models. Instead, at the front part of the jet near its head is the fastest and most energetic fluid whose velocity is almost in the radial direction, while at the sides of the jet there is slower and less energetic fluid whose velocity is not in the radial direction but points more sideways.[3] This slower material at the sides of the jet dominates the emission at early times for large viewing angles $\theta_{\rm obs}$, since its emission has a much wider beaming cone and covers a larger solid angle, as compared to the material at the front of the jet, which has a much larger Lorentz factor Γ and its velocity is almost in the radial direction, so that its radiation is strongly beamed away from observers at large off-axis viewing angles (Granot et al. 2001, 2002; Granot 2007; Zhang & MacFadyen 2009; van Eerten & MacFadyen 2011; De Colle et al. 2012b).

Fig. 6 shows afterglow light curves from 2D relativistic hydrodynamic simulations of a GRB jet following De Colle et al. (2012a,b). The initial conditions feature a conical wedge of initial half-opening angle $\theta_0 = 0.2$ from the Blandford & McKee (1976, BM76 hereafter) self-similar solution, with a true energy (for a double-sided jet) of $E = 10^{49}$ erg (corresponding to an isotropic equivalent kinetic energy of $E_{k,\rm iso} \approx 5 \times 10^{50}$ erg), and an external density of $n = 1\,{\rm cm}^{-3}$ (i.e. $n_0 = 1$). The light curves for observers located at different viewing angles $\theta_{\rm obs}$ from the jet's symmetry axis are calculated following the hydrodynamic simulation of the jet dynamics, where we have set $\varepsilon_{\rm e} = \varepsilon_B = 0.1$ and $p = 2.5$ for the values of the shock microphysical parameters.

It can be seen that the light curves for larger viewing angles $\theta_{\rm obs}$ peak at a later time and at a lower flux level. For a given $\theta_{\rm obs}$, after the light curve peaks it approaches that for an on-axis observer, since the jet's beaming cone engulfs the line of sight. At very late times when the flow becomes Newtonian the light curves become essentially independent of the viewing angle $\theta_{\rm obs}$ since relativistic beaming and light travel effects become unimportant. Around the non-relativistic transition time there is a bump in the light curve as the emission from the counter-jet becomes visible and at its peak it is somewhat brighter than the jet that points more towards us since relativistic beaming becomes small, and due to light travel effects, we are seeing its emission from a smaller radius (compared to that of the forward jet at the same observed time) where it was intrinsically brighter.

Fig. 7 compares afterglow light curves from numerical simulations to the analytic predictions for the peak time and flux as describes in Section 3 and Section 4. In the optical and X-ray (where the on-axis light curves decay at early times) the light curves from viewing angles slightly outside of the jet $\theta_0 < \theta_{\rm obs} \lesssim (2-3)\theta_0$ peak earlier than the analytic predictions due to some lateral spreading of the jet and the slower material on its sides that both cause the jet's beaming cone to reach such viewing angles faster than the analytic expectations. For larger viewing angles, $\theta_0 \sim 0.8$–1 in our case, the light curves peak later than the analytic expectation since the jet expands sideways and decelerates much more slowly with radius and observed time compared to the analytic models that feature

[3]The direction velocity of the fluid just behind the shock is in the direction of the local shock normal in the rest frame of the upstream fluid, i.e. that of the circumstellar medium and central source (from the shock jump conditions, as pointed out, e.g. by Kumar & Granot 2003).

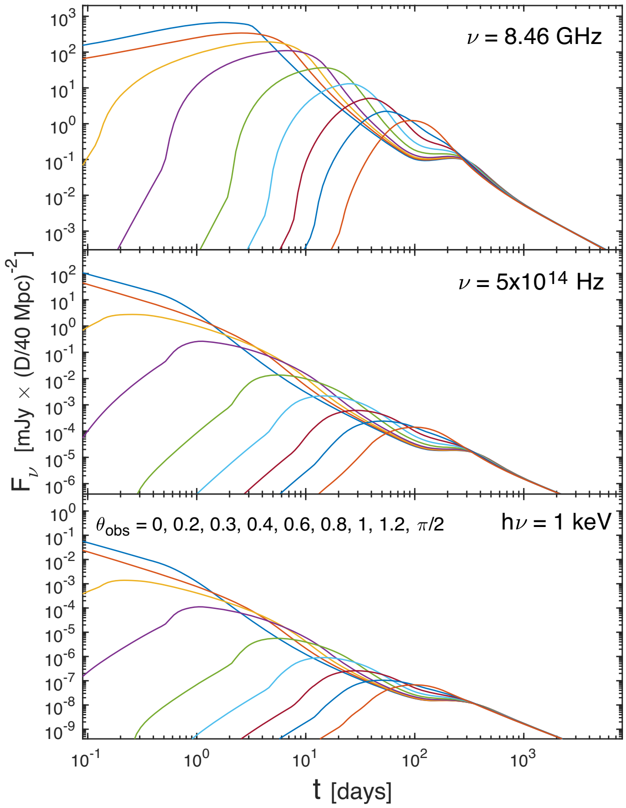

Figure 6. Afterglow light curves from numerical simulations for different viewing angles $\theta_{\rm obs}$ from the jet's symmetry axis, in the radio (*upper panel*), optical (*middle panel*), and X-ray (*bottom panel*). The simulations follow De Colle et al. (2012a,b) and are for an external density $n_0 = 1$, true (double-sided) jet energy of $E = 10^{49}$ erg, initial jet half-opening angle of $\theta_0 = 0.2$, as well as $\varepsilon_e = \varepsilon_B = 0.1$ and $p = 2.5$. The flux normalization is for a distance of $D = 40$ Mpc to the source. Note that there is an artificially sharp increase in the rate of flux rise (i.e. a sharp corner in the light curve) corresponding to the observed time of the transition from being dominated by the early BM76 conical wedge to the hydrodynamic simulation.

an exponential lateral expansion, and therefore its beaming cone reaches large $\theta_{\rm obs}$ at later times. The analytic peak flux prediction is higher than that from numerical simulations by roughly an order of magnitude. The numerical flux at the analytic peak time is even somewhat below the numerical peak flux (sometimes by more than an order of magnitude; see the dots in Fig. 7 that are a factor of 10 lower flux than the analytic peak flux) since the numerical peak time generally deviates from the analytic prediction as discussed above.

In the radio, the peak of the off-axis light curves occurs significantly later. At the time when the line of sight enters the jet's beaming cone there is a flattening in the light curve but since the on-axis light curve still rises in the radio then unlike in the optical and X-ray where this is enough for the flux to start decaying at that time (so that it corresponds to the peak time), in the radio the flux continues to gently rise. The radio flux peaks and starts to decay only around the time when the break frequency $\nu_{\rm m}$ crosses the observed radio frequency (which is observed at somewhat different times for different viewing angles $\theta_{\rm obs}$). In this case, using $A = 2.5$ gives a better fit for the peak time and flux (compared to $A = 1$).

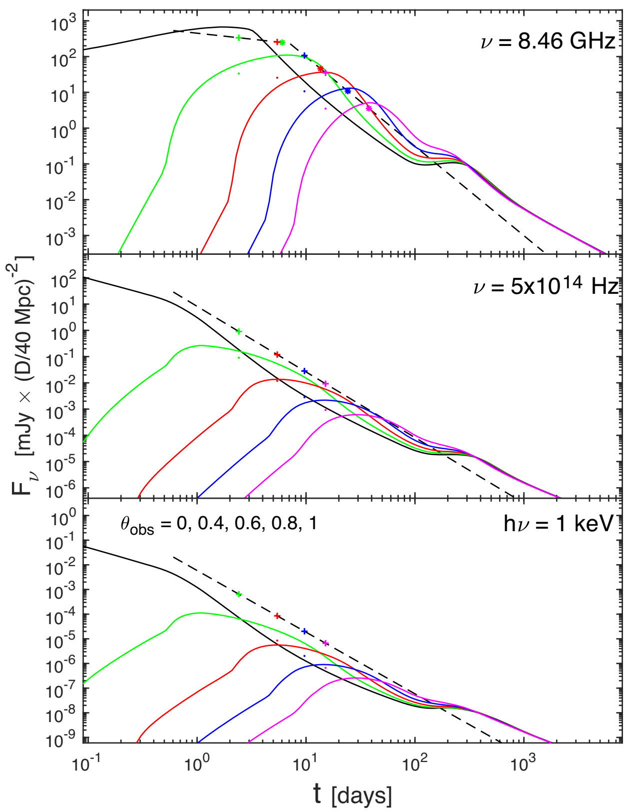

Figure 7. Similar to Fig. 6 but showing fewer viewing angles and superimposing the analytic predictions for the peak time and flux as describes in Sections 3 and 4. The plus signs are according to equation (9) with $A = 1$ and are along the dashed black line indicating the analytic on-axis flux. The dots are a factor of 10 lower flux. For the radio (*top panel*), we also show asterisks (with the same colour coding for the different viewing angles $\theta_{\rm obs}$) corresponding to $A = 2.5$.

6 CONSTRAINING THE JET PHYSICAL PARAMETERS FROM GRB 170817A DATA

6.1 General considerations from the prompt emission

Granot et al. (2017) have argued that the relatively low measured values of the isotropic equivalent γ-ray energy output, $E_{\gamma,\rm iso} = (5.36 \pm 0.38) \times 10^{46} D^2_{40\,\rm Mpc}$ erg, and the peak νF_ν photon energy, $E_{\rm p} \sim 40$–185 keV, measured for GRB 170817A favour an off-axis viewing angle outside of the jet's initial aperture ($\theta_{\rm obs} > \theta_0$) (also see e.g. Alexander et al. 2017; Margutti et al. 2017; Murguia-Bertier et al. 2017; Troja et al. 2017). Comparison of these values to those typical of other short-hard GRBs (that are viewed from within the jet's initial aperture with $\theta_{\rm obs} < \theta_0$) implies that for a uniform sharp-edged jet our line of sight is only slightly outside of the jet $\Delta\theta = \theta_{\rm obs} - \theta_0 \sim (0.05$–$0.1)(100/\Gamma_0)$, which would in turn imply an unusually high on-axis $E_{\rm p} \sim 3$–8 MeV (or ∼5–20 MeV for the main half-second initial spike; Granot et al. 2017; Abbott et al. 2017e). Such a viewing angle would also imply an early peak for the afterglow light curve, since the beaming cone would reach the line of sight within $t_{\rm peak} \lesssim 1$ d, when $\Gamma(t_{\rm peak}) \approx 1/\Delta\theta \sim (10$–$20)(\Gamma_0/100)$ (see equation 18). Since such an early peak of the afterglow emission was not seen in GRB 170817A, this scenario is disfavoured.

An alternative scenario that was favoured by Granot et al. (2017) is that of a 'structured jet', which does not have sharp edges but instead a roughly uniform core of half-opening angle θ_0 outside of which the energy per unit solid angle and Γ drops gradually, rather than abruptly. In this case, the prompt GRB is dominated by the emission from material along our line of sight, which is well outside of the jet's core angle ($\theta_{\rm obs} \gtrsim 2\theta_0$) and correspondingly less energetic. This would imply a higher afterglow flux at early times compared to a sharp-edged jet, arising from the material along our line of sight. Furthermore, as more energetic material at $\theta < \theta_{\rm obs}$ slows down and its beaming cone widens, its emission starts contributing to the flux in the observer's LOS. This results in a gradual rise of the afterglow to the peak at which point the core of the jet is visible. The contribution to the early afterglow flux from the material along our line of sight, assuming $E_{k,\rm iso}(\theta = \theta_{\rm obs}) \sim E_{\gamma,\rm iso}$ is consistent with observations (i.e. it does not exceed the observed flux or upper limits; Granot et al. 2017).

6.2 Comparison with observations of afterglow light curves from an off-axis initially top-hat relativistic jet

In this section, we compare the predicted afterglow emission from a GRB jet viewed off-axis to the observations of GRB 170817A. We calculate the flux from the jet's core and the wings that is produced as a result of its interaction with the external medium by using the results of hydrodynamic simulations for the jet dynamics during the afterglow phase (De Colle et al. 2012a,b). These simulations use as initial conditions a conical wedge taken out of the spherical self-similar BM76 solution. This is the sharpest-edged jet one can take (with a step function at $\theta = \theta_0$), but still on the dynamical time it develops wings of slower and less energetic material on its sides, at large angles θ, whose emission is less beamed than that from its energetic core (at $\theta < \theta_0$). Therefore, a top-hat jet inevitably transforms into a structured jet (Granot et al. 2001).

The numerical light curves are calculated by post-processing the results of the hydrodynamic simulation. However, calculating the light curves for a very large number of sets of parameter values would require huge computational resources. This is a serious issue not only when varying all of the free parameters (E, n, $\varepsilon_{\rm e}$, ε_B, p, $\theta_{\rm obs}$, and θ_0), but even when varying only a subset of them. We address this issue as follows. First, we use the results of a single hydrodynamic simulation for $\theta_0 = 0.1$, $n_0 = 1$, and $E_{\rm k,\,iso} = 5 \times 10^{50}$ erg corresponding to $E = (1 - \cos\theta_0)E_{k,\rm iso} \approx E_{k,\rm iso}\theta_0^2/2 = 2.5 \times 10^{48}$ erg, and rescale them to arbitrary values of n_0 and E using the scaling relations described in Granot (2012a). Since θ_0 cannot be rescaled it remains fixed at $\theta_0 = 0.1$. Secondly, we also use the fully analytic scaling of the flux density within any given power-law segment (PLS) of the afterglow synchrotron spectrum with all of the model parameters, as summarized in table 2 of Granot (2012a). A broadly similar approach was used, e.g. by van Eerten & MacFadyen (2012) and Ryan et al. (2015).

We have calculated the light curves at a single observed frequency, which was assumed in turn to always be within one of the relevant PLSs (PLSs D, G, and H using the notations of Granot & Sari 2002), where each PLS is fully rescalable as discussed above. For each PLS, we calculated the light curves for a large number of viewing angles in the range $\theta_{\rm obs} \in [0, \pi/2]$, and then interpolated between these values for any arbitrary viewing angle. Since the spectrum is convex, a broken power-law approximation of the spectrum is simply obtained by using the minimal flux out of that for all of the relevant PLSs. The spectrum can be refined to a more realistic shape that is smooth near the break frequencies using, e.g. the prescriptions from Granot & Sari (2002). In the case of GRB 170817A, it has been found (e.g. Hallinan et al. 2017; Margutti et al. 2018) that all observations of the afterglow, from radio to X-rays, lie on a single PLS G with $\nu_{\rm m} < \nu < \nu_{\rm c}$. Afterglow observations of this event thus far suggest that the cooling break has not yet entered the X-ray band (Nynka et al. 2018).

Our aim is to test whether an initially top-hat jet model viewed off-axis can adequately fit the afterglow data. The model parameter used in the fit are the jet's true energy E, the external density n, our viewing angle $\theta_{\rm obs}$, and the shock microphysical parameters $\varepsilon_{\rm e}$, ε_B, and p. We make use of the up to date radio, X-ray, and late optical data for fitting (e.g. Alexander et al. 2018; Margutti et al. 2018 and references therein; Haggard et al. 2018; Mooley et al. 2018b; Rossi et al. 2018).

An important feature that occurs in light curves calculated from simulations is caused by their finite start time. The latter leads to a finite observed time when any (and shortly thereafter the dominant) contribution to the observed flux from the finite simulated space-time region reaches the observer. Before this time it does not make physical sense to fit the light curve to the observed data. For this reason, such numerical afterglow light curves are often supplemented by emission from a conical wedge taken out of the spherical self-similar BM76 solution at earlier lab frame times, before the onset of the simulation. The emission from the BM76 wedge leads to a sharp power-law flux rise at early times. Once the emission from the simulation reaches the observer its flux quickly dominates and initially causes a sharp flux increase. This is followed by a slower flux rise after a single dynamical time, once the dynamics in the simulation have relaxed from the initial conditions (see e.g. Figs 6 and 7, as well as Bietenholz et al. 2014). This sharp feature is an artefact of initializing the hydrodynamic simulation at a finite lab-frame time, which usually corresponds to a modest initial Lorentz factor (in our case $\Gamma_0 = 20$). A companion paper (Gill et al. in preparation) explores the effects of the finite simulation start time or the corresponding Γ_0.

In the present work, the light curve fitting is guided by the measured peak of the afterglow observations at $t_{\rm pk} \sim 150$ d and the data points just before and after the peak. In Fig. 8, we show the fit to the afterglow data that has been normalized in all energy bands to the corresponding flux at 3 GHz. We do not attempt to fit the early time data at $t \lesssim 40$ d, before the model light curves contain the dominant and dynamically relaxed contribution from the finite simulated space-time region. Moreover, for this reason we do not show the model light curves at these early times (grey shaded region in Fig. 8). Taking this into account we obtain a reasonable fit to the afterglow data. The model parameters of this fit are: a true jet energy $E \approx 10^{50.3}$ erg, circumburst density $n_0 \approx 10^{-3.6}$, viewing angle $\theta_{\rm obs} \approx 0.3$ rad (17.2°), and afterglow shock micro-physical parameters $\varepsilon_{\rm e} \approx 10^{-1.8}$, $\varepsilon_B \approx 10^{-3}$, and $p \approx 2.16$. Broadly similar values of some of the model parameters were also obtained in recent works that explored models of structured jets (e.g. Gill & Granot 2018; Margutti et al. 2018; Troja et al. 2018; Xie et al. 2018). Our fit can best constrain: (i) $p \approx 2.16$ (thanks to the well-measured radio to X-ray spectral slope), and (ii) the ratio of the viewing angle and jet initial half-opening angle, $\theta_{\rm obs}/\theta_0 \approx 3$ (since it significantly affects the shape of the light curve before and around the peak time).

However, since the model parameters outnumber the effective constraints from the data, a significant degeneracy remains between the different model parameters. Therefore, the model fit we present to the data only illustrates one possible set of model parameters that can explain the observations. Moreover, even for ideal data there is a degeneracy that still remains. As shown by Eichler & Waxman (2005), the afterglow flux is invariant under the change $E \to E/\xi_{\rm e}$, $n \to n/\xi_{\rm e}$, $\varepsilon_{\rm e} \to \varepsilon_{\rm e}\xi_{\rm e}$, and $\varepsilon_B \to \varepsilon_B\xi_{\rm e}$, for $m_{\rm e}/m_{\rm p} < \xi_{\rm e} \leq 1$, where $\xi_{\rm e}$ is the fraction of electrons that are shock accelerated to the relativistic power-law energy distribution considered in most works. This degeneracy can only be broken through the effect of the remaining electrons that are typically expected to form a thermal distribution (e.g. Eichler & Waxman 2005; Giannios & Spitkovsky 2009; Ressler & Laskar 2017). Here, we assume $\xi_e = 1$.

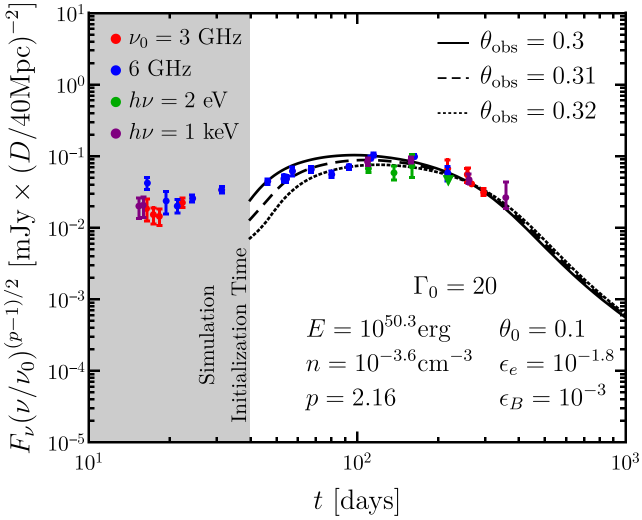

Figure 8. Comparison of the afterglow light curve from an initially top-hat jet with observations, shown here for three different viewing angles. Observations in different energy bands have been normalized to the corresponding flux at $\nu_0 = 3$ GHz. The upper limit in the optical is shown by a downward triangle. The sharp flux rise at $t \lesssim 50$ d is caused by the finite simulation start time, which corresponds to an unrealistically low initial LF $\Gamma_0 = 20$. Therefore, no realistic model predictions are currently available in the grey shaded region (this would require significantly larger Γ_0 values, which are computationally very challenging).

7 SUMMARY

In this work, we have first briefly described the IR, optical, and UV emission from half a day up to about a few weeks after the event (in Section 2). Its quasi-thermal spectrum as well as peak time and temperature favour a kilonova origin with two distinct components. The first which powered the 'blue' kilonova is explained by a faster moving ($\beta_{\rm ej} \approx 0.3$) Lanthanide-poor ejecta. The second component which powered the 'red' kilonova is instead explained by a slower moving ($\beta_{\rm ej} \approx 0.1$) Lanthanide-rich ejecta.

In the Appendix, we used the measured offset of the optical/IR emission from the centre of NGC 4993, of $r_\perp = 2$ kpc, to constrain the distance $s = v_{\rm sys}t_{\rm mer} \lesssim 2-10$ kpc travelled by the NS-NS system from its birth to its merger location, assuming straight-line motion. Given the old stellar ages in elliptical galaxies, we find that one must account for the galaxy's gravitational potential and integrate the binary's possible trajectories in order to make more reliable quantitative inferences from $r_\perp$. Detailed kinematic modelling in Abbott et al. (2017c) of the progenitor binary NS from the second supernova to the merger time constrained the birth site of the compact binary to a radial distance of $\simeq 2.0^{+4.0}_{-1.5}$ kpc from the galactic centre and systemic velocity to $\simeq 250$ km s^{-1} for a merger time $t_{\rm mer} > 1$ Gyr.

We have presented (in Section 3) a simple analytic model for the peak time ($t_{\rm peak}$) and flux ($F_\nu^{\rm peak}$) of the afterglow emission from viewing angles outside of the jet's initial aperture ($\theta_{\rm obs} > \theta_0$), as well as the flux evolution after the peak, and provided general predictions of this model (for $\theta_{\rm obs} \gtrsim 2\theta_0$; in Section 4).

It was then contrasted with the results of numerical light curves from hydrodynamic simulations of the GRB jet during the afterglow phase (in Section 5). In the X-ray and optical, where the on-axis light curves decay at early times, the light curves from viewing angles mildly outside of the initial jet aperture, $\theta_0 < \theta_{\rm obs} \lesssim (2$–$3)\theta_0$, were found to peak earlier than the analytic predictions (due to slower material on the sides of the jet and some lateral spreading, which causes the jet's beaming cone to reach such $\theta_{\rm obs}$ faster than the analytic expectations), while for larger $\theta_{\rm obs}$ the light curves peak later than the analytic expectation (since the jet decelerates and expands sideways more slowly with radius and observed time compared to the analytic models that feature an exponential lateral expansion with radius, and hence its beaming cone reaches large $\theta_{\rm obs}$ at later times). The analytic prediction for the peak flux is higher than that from numerical simulations by roughly an order of magnitude, since the numerical peak time occurs somewhat before the off-axis light curve join the on-axis light curve, while in the analytic model the two are assumed to coincide.

In the radio, since the on-axis light curve still rises when the beaming cone reaches the line of sight, the flux continues to gently rise, and it starts to decay only near the passage of ν_m, which is observed at somewhat different times for different viewing angles $\theta_{\rm obs}$, thus resulting in later peak times. The discrepancy in peak flux is smaller (see the upper panel of Fig. 7).

The numerical afterglow light curves from hydrodynamic simulations were directly contrasted with the data for GRB 170817A in Section 6. Up to date afterglow data in radio, optical, and X-rays was used for the fitting, and the early IR to UV data were not included as they are dominated by the kilonova emission. In order to allow more efficient fits to the data given the reasonably large number of model parameters and corresponding parameter space to explore, we have made use of two types of scaling relations (following Granot 2012a): (i) of the dynamical equations, by arbitrary rescaling the energy and density in order to avoid the need for performing a large number of hydrodynamic simulations, and (ii) additional scalings of the flux density within each of the different power-law segments of the afterglow synchrotron spectrum (with the shock microphysics parameters), in order to greatly reduce the number of required numerical light curve calculations.

We fit the afterglow data and find that it can be explained by a viewing angle to jet initial half-opening angle ratio of $\theta_{\rm obs}/\theta_0 \approx 3$, where in our simulations $\theta_0 = 0.1 = 5.7^\circ$ (we also obtained a similarly good fit with $\theta_{\rm obs}/\theta_0 \approx 3$ for $\theta_0 = 0.2$).

8 DISCUSSION

The new discovery of the first GW signal from the merger of a binary NS system, which was also accompanied by a SGRB, GRB 170817A, solidifies the role of binary NS mergers as the progenitors of SGRBs. Moreover, it also opens a new window in multi-messenger astronomy that enables us to learn more about SGRB physics. The great interest that this has raised in the community resulted in an exquisite follow-up campaign, which allows us to learn about the properties of the outflow generated in the course of this explosive event.

After this paper was submitted more data became available and more modelling was performed. Structured jet afterglow models, based either on semi-analytic formulations (D'Avanzo et al 2018; Gill & Granot 2018; Lamb & Kobayashi 2018; Resmi et al. 2018; Troja et al. 2018) or on numerical simulations (Lazzati et al. 2018; Margutti et al. 2018; Xie et al. 2018), have been successful at explaining the observations up to and including the peak of the light curves. The numerical models give a steeper flux decay after the peak, which better agrees with the late time data.

An alternative model that was proposed to explain the long-lasting rise of the afterglow flux was that of a wide-angle quasi-spherical cocoon shock breaking out of either the dynamical ejecta of the NS–NS merger or the shocked relativistic wind (Lazzati et al. 2017b; Gottlieb et al. 2018; Kasliwal et al. 2017; Mooley et al. 2018a; Nakar & Piran 2018). In this scenario, the jet may either be chocked or successfully break out. In either case, the outflow develops a broad distribution of energy with proper velocity $u = \Gamma\beta$, where most of the energy resides in the slower moving material. Ejecta of a given u catches up with the afterglow shock and energizes it when it decelerates to slightly below u, thus leading to continuous energy injection into the afterglow shock (Sari & Mészáros 2000; Nakamura & Shigeyama 2006). This can occur largely independently at each angle θ from the outflow's symmetry axis. The resulting energy injection into the afterglow shock along the observer's LOS may account for the observed flux rise if it is fast enough. This effect of the radial profile may dominate over the outflow's angular profile.

Both the radial energy distribution with u or angular energy distribution with θ (structured jet) yielded similar afterglow light curves, which were able to fit the observations up to the peak. It was in the post-peak predictions where the two models differed from each other. Here, the structured jet models showed a steeper decline of the light curve as compared to the shallower decay obtained from quasi-spherical models that are dominated by their radial structure. Recent observations of the afterglow post-peak show a steep decline, and therefore favour a structured jet scenario. However, this conclusion is not very robust and further observations will shed more light on this issue.

In order to discriminate between the two competing types of models Gill & Granot (2018) provide three additional diagnostics, namely the polarization, flux centroid motion, and afterglow image size and axial ratio, which can help to break the degeneracy. Recent radio observations at 2.8 GHz by Corsi et al. (2018) were used to place an upper limit of ≈12 per cent (with 99 per cent confidence) on the level of linear polarization at ≈244 d post-merger. However, the predicted polarization depends not only on the outflow's angular structure, but also on the local magnetic field structure within the shocked external medium behind the afterglow shock. Therefore, this polarization upper limit provided a combined constraint on both, rather than on each of them separately. Recent Very Long Baseline Array radio observations by Mooley et al. (2018b) were used to measure the angular motion of the flux centroid over 155 d (between 75 and 230 d post-merger) to be $\Delta\theta_{\rm fc} = 2.73 \pm 0.3$ mas, as well as to set an upper limit on the radio afterglow's angular size. This flux centroid motion corresponds to a super-luminal apparent proper velocity of $4.1 \pm 0.5c$. When compared to the prediction of Gill & Granot (2018) for the flux centroid motion for the two different types of models, it clearly rules out any wide-angle quasi-spherical flow model and instead favours a structured jet model. This implies a narrow jet with most of its energy residing within a narrow core (of half-opening angle $\lesssim 0.1$).

Such a narrow, core-dominated jet is consistent with the initially top-hat jet that we use in the simulations presented in this work. It is broadly consistent with all of the afterglow observations, including both the X-ray to radio light curves as well as the flux centroid motion and upper limit on the size of the radio afterglow image. Similar initially top-hat jet models were used to fit the afterglow data in many works (e.g. Troja et al. 2017; Lazzati et al. 2018; Margutti et al. 2018; Mooley et al. 2018a). However, such a model was discarded since it was argued to produce an early ($t \lesssim 40$ d) flux rise that is steeper than observed. In particular, it was found that a top-hat jet model yields steeply rising light curves ($F_\nu \propto t^\alpha$ with $\alpha \sim 3$–4), whereas the data showed a much shallower rise to the peak ($F_\nu \propto t^{0.8}$). However, the early steeply rising light curve arises from the contribution of a BM76 conical wedge at lab frame times before the simulation onset, as well as from the first dynamical time after the simulation onset, before the jet relaxes from its initial conditions by forming a bow-shock like structure. Therefore, this part is not very physical, and is instead an artefact due to the finite simulation start time. When using the part of the light curve dominated by the contribution from the simulation and excluding the first dynamical time where the jet relaxes from its initial conditions, we find an acceptable fit to the afterglow light curves.

ACKNOWLEDGEMENTS

We thank E. Sobacchi, E. Behar, and L. Yacobi for useful discussions. JG and RG acknowledge support from the Israeli Science Foundation under Grant No. 719/14. RG is supported by an Open University of Israel Research Fellowship.

REFERENCES

Abbott B. P. et al., 2016a, Phys. Rev. Lett., 116, 061102
Abbott B. P. et al., 2016b, ApJ, 832, 21
Abbott B. P. et al., 2017a, Phys. Rev. Lett., 119, 141101
Abbott B. P. et al., 2017b, Phys. Rev. Lett., 119, 161101
Abbott B. P. et al., 2017c, ApJ, 850, L40
Abbott B. P. et al., 2017d, ApJ, 848, L12
Abbott B. P. et al., 2017e, ApJ, 848, L13
Alexander K. D. et al., 2017, ApJ, 848, L21
Alexander K. D. et al., 2018, ApJ, 863, L18
Arcavi I. et al., 2017, Nature, 551, 64
Belczynski K., Perna R., Bulik T., Kalogera V., Ivanova N., Lamb D. Q., 2006, ApJ, 648, 1110
Berger E., 2014, ARA&A, 52, 43
Bietenholz M. F., De Colle F., Granot J., Bartel N., Soderberg A. M., 2014, MNRAS, 440, 821
Blandford R. D., McKee C. F., 1976, Phys. Fluids, 19, 113
Corsi A. et al., 2018, ApJ, 861, L10
Coulter D. A. et al., 2017, Science, 358, 1556
Cowperthwaite P. S. et al., 2017, ApJ, 848, L17
De Colle F., Granot J., Lopez-Camara D., Ramirez-Ruiz E., 2012a, ApJ, 746, 122
De Colle F., Ramirez-Ruiz E., Granot J., Lopez-Camara D., 2012b, ApJ, 751, 57
Drout M. R. et al., 2017, Science, 358, 1570
D'Avanzo P. et al., 2018, A&A, 613, L1
Eichler D., Granot J., 2006, ApJ, 641, L5
Eichler D., Livio M., Piran T., Schramm D. N., 1998, Nature 340, 126
Eichler D., Waxman E., 2005, ApJ, 627, 861
Evans P. A. et al., 2017, Science, 358, 1565
Fong W., Berger E., Margutti R., Zauderer B. A., 2015, ApJ, 815, 102
Giannios D., Spitkovsky A., 2009, MNRAS, 400, 330
Gill R., Granot J., 2018, MNRAS, 478, 4128
Gottlieb O., Nakar E., Piran T., 2018, MNRAS, 473, 576
Granot J., 2007, Rev. Mex. Astron. Astrofis., 27, 140
Granot J., 2012a, MNRAS, 421, 2610
Granot J., 2012b, MNRAS, 421, 2442
Granot J., Guetta D., Gill R., 2017, ApJ, 850, L24
Granot J., Panaitescu A., Kumar P., Woosley S. E., 2002, ApJ, 570, L61
Granot J., Piran T., 2012, MNRAS, 421, 570
Granot J. , Ramirez-Ruiz E. , 2012, in Woosley S. E., Wijers R. A. M. J., eds, Jets and Gamma-ray Burst Unification Schemes, Chap. 11, Gamma-ray Bursts. Cambridge Univ. Press, Cambridge
Granot J., Sari R., 2002, ApJ, 568, 820
Granot J. Miller M. Piran T. Suen W. M. Hughes P. A., Costa E., Frontera F., Hjorth J., 2001, eds, GRBs in the Afterglow Era. Berlin, Springer, p. 312
Gruzinov A., 2007, preprint (arXiv:0704.3081)
Haggard D., Nynka M. , Ruan J., 2018, GCN Circulars 23137
Hallinan G. et al., 2017, Science, 358, 1579
Hansen B. M. S., Lyutikov M., 2001, MNRAS, 322, 695
Hernquist L., 1990, ApJ, 356, 359
Kasen D., Fernandez R., Metzger B. D., 2015, MNRAS, 450, 1777
Kasen D., Metzger B., Barnes J., Quataert E., Ramirez-Ruiz E., 2017, Nature, 551, 80
Kasliwal M. M. et al., 2017, Science, 358, 1559
Keshet U., Kogan D., 2015, ApJ, 815, 100
Kilpatrick C. D. et al., 2017, Science, 358, 1583
Kumar P., Granot J., 2003, ApJ, 591, 1075
Kyutoku K., Ioka K., Shibata M., 2014, MNRAS, 437, L6
Lamb G. P., Kobayashi S., 2018, MNRAS, 478, 733
Lattimer J. M., Schramm D. N., 1976, ApJ, 210, 549
Lazzati D., Deich A., Morsony B. J., Workman J. C., 2017a, MNRAS, 471, 1652
Lazzati D., L´ópez-Cámara D., Cantiello M., Morsony B. J., Perna R., Workman J. C., 2017b, ApJ, 848, L6
Lazzati D., Perna R., Morsony B. J., Lopez-Camara D., Cantiello M., Ciolfi R., Giacomazzo B., Workman J. C., 2018, Phys. Rev. Lett., 120, 241103
Li L.-X., Paczyński B., 1998, ApJ, 507, L59
Margutti R. et al., 2017, ApJ, 848, L20
Margutti R. et al., 2018, ApJ, 856, L18
Metzger B. D., 2017, LRR, 20, 3
Metzger B. D., Fernandez R., 2014, MNRAS, 441, 3444
Metzger B. D. et al., 2010, MNRAS, 406, 2650
Mooley K. P. et al., 2018a, Nature, 554, 207
Mooley K. P. et al., 2018b, preprint (arXiv:1806.09693)
Murguia-Berthier A. et al., 2017, ApJ, 848, L34
Nakamura K., Shigeyama T., 2006, ApJ, 645, 431
Nakar E., 2007, PhR, 442, 166
Nakar E., Piran T., 2011, Nature, 478, 82
Nakar E., Piran T., 2017, ApJ, 834, 28
Nakar E., Piran T., 2018, MNRAS, 478, 407
Nakar E., Piran T., Granot J., 2002, ApJ, 579, 699
Narayan R., Paczynski B., Piran T., 1992, ApJ, 395, L83
Nynka M., Ruan J. J., Haggard D., Evans P. A., 2018, ApJ, 862, L19
Pian E. et al., 2017, Nature, 551, 67
Piran T., 2000, Phys. Rep., 333, 529
Resmi L. et al., 2018, preprint (arXiv:1803.02768)
Ressler S. M., Laskar T., 2017, ApJ, 845, 150
Rezzolla L., Giacomazzo B., Baiotti L., Granot J., Kouveliotou C., Aloy M. A., 2011, ApJ, 732, L6
Rhoads J. E., 1997, ApJ, 487, L1
Rhoads J. E., 1999, ApJ, 525, 737
Rossi A. et al., 2018, GCN Circular 22763
Rosswog S., Piran T., Nakar E., 2013, MNRAS, 430, 2585
Ryan G., van Eerten H., MacFadyen A., Zhang B.-B., 2015, ApJ, 799, 3
Sari R., Mészáros P., 2000, ApJ, 535, L33
Sari R., Piran T., Halpern J. P., 1999, ApJ, 519, L17
Sari R., Piran T., Narayan R., 1998, ApJ, 497, L17
Shappee B. J. et al., 2017, Science, 358, 1574
Smartt S. J. et al., 2017, Nature, 551, 75
Troja E. et al., 2017, Nature, 551, 71
Troja E. et al., 2018, MNRAS, 478, L18
van Eerten H. J., MacFadyen A. I., 2011, ApJ, 733, L37
van Eerten H. J., MacFadyen A. I., 2012, ApJ, 747, L30
von Kienlin A., Meegan C., Goldstein A., 2017, GCN, 21520, 1
Woosley S. E., Bloom J. S., 2006, ARA&A, 44, 507
Wygoda N., Waxman E., Frail D. A., 2011, ApJ, 738, L23

Xie X., Zrake J., MacFadyen A., 2018, ApJ, 863, 58
Zhang B., 2014, ApJ, 780, L21
Zhang W., MacFadyen A. I., 2009, ApJ, 698, 1261

APPENDIX A: GRB 170817A'S LOCATION WITHIN ITS HOST GALAXY

Here we try to determine if the position of the source in the host galaxy can be explained as a straight-line motion from the birth site of the binary to its merger site using a simple likelihood analysis. GRB 170817Ais located $r_\perp \simeq 2$ kpc in projection on to the plane of the sky from the centre of the elliptical galaxy NGC 4993. We use $r_\perp$ to constrain the distance $s = v_{\rm sys}t_{\rm mer}$ travelled by the binary over its lifetime $t_{\rm mer}$ from its birth location $\vec{r}_i$ to that of merger, $\vec{r}_f = \vec{r}_i + \vec{s}$, assuming a straight-line motion at a systemic velocity $v_{\rm sys}$, via a likelihood analysis based on the stellar mass distribution in elliptical galaxies (approximated here as spherical). For initial and final galactocentric radii r_i and $r_f = \sqrt{s^2 + r_i^2 - 2sr_i\mu}$, where $\mu = -(\vec{r}_i \cdot \vec{s})/r_i s$, the probability density function of s can be expressed as

$$P(s) \propto \int_0^\infty {\rm d}r_i\, P(r_i) \int_{|r_i-s|}^{r_i+s} {\rm d}r_f\, P(r_f|r_i, s) f_\Omega(f_f). \tag{A1}$$

Its normalization is obtained by requiring $\int P(s){\rm d}s = 1$. The distribution of birth locations follows that of the stellar mass in the host galaxy given here by the Hernquist (1990) profile such that $P(r_i) = {\rm d}\ln M(r_i)/{\rm d}r_i = 2r_i a/(r_i + a)^3$, where the effective radius is $r_{\rm e} \approx 1.8153a$. Given r_i and s, the conditional probability for r_f for an isotropic $P(\mu) = \frac{1}{2}$ is $P(r_f|r_i, s) = r_f/(2sr_i)$. Finally, given r_f the fraction of observers (or total solid angle) that would see an offset $\leq r_\perp$ is $f_\Omega = 1 - \mu_\theta$ with $\mu_\theta = \sqrt{1 - (r_\perp/r_f)^2}$ for $r_f \geq r_\perp$ and $f_\Omega = 1$ for $r_f < r_\perp$. Fig. A1 shows $P(s)$ along with the cumulative fraction of such binaries found within s for two r_e values bracketing the range typical for elliptical galaxies. This suggests that the binary has travelled a rather modest distance of $s \lesssim 2$–10 kpc from its birth location. The distribution of merger times $t_{\rm mer}$ (including formation of the compact binary) is rather flat between 10 Myrand10 Gyr with a conspicuous peak at 20 Myr due to very tight orbit binaries (Belczynski, Perna & Bulik 2006). Since in most elliptical galaxies active star formation ceased at $z \approx 2$, the binary cannot be too young and must have $t_{\rm mer} > 1$ Gyr. Such a long-lived binary would in turn imply a very small systemic velocity, $v_{\rm sys} = s/t_{\rm mer} \lesssim (2$–$10)(t_{\rm mer}/1\,{\rm Gyr})^{-1}$ km s^{-1}, which is much smaller than both the expectation for a natal kick (population synthesis studies find $\langle v_{\rm kick}\rangle \sim 50$–100 km s^{-1}, while larger values are often inferred from observations) and systemic velocities of stars in massive elliptical galaxies ($\gtrsim$200 km s^{-1}). Therefore, the assumption of straight-line motion cannot hold in this case. This can also be seen from the fact that the Keplerian times of the host galaxy's stars are typically much less than their ages (i.e. many galactic orbits were completed since the last star formation epoch). One must therefore account for the host galaxy's gravitational potential, which requires orbit-tracking numerical calculations. Such an effect is naturally incorporated in a population synthesis scheme that is outside the scope of this work, but see the work by Abbott et al. (2017c), where kinematic modelling of the progenitor binary NS was done.

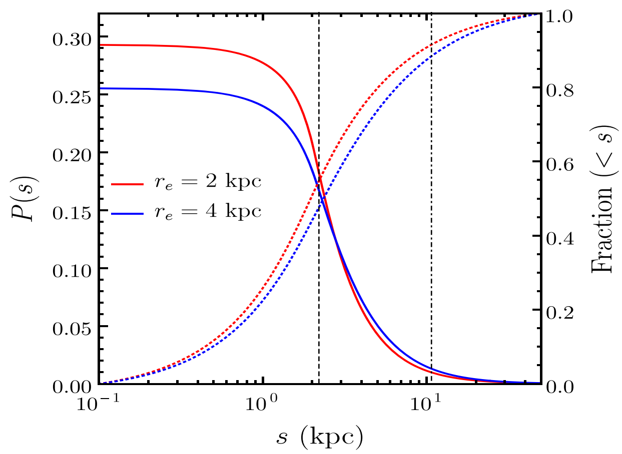

Figure A1. Probability ($P(s)$) of the binary having travelled distance s from birth to merger locations (solid) and the cumulative distribution $\int_0^s P(s'){\rm d}s'$ (dotted) shown for two effective radii $r_{\rm e}$. The median and the distance containing 90 per cent of the mergers, both averaged over the two cases, are shown as dashed and dot–dashed lines.

This paper has been typeset from a TEX/LATEX file prepared by the author.